

# Rare Earth 2-Methyl-3-furoate Complexes: Effect of Steric Hindrance on Corrosion Inhibitor Properties

Vidushi P. Vithana,<sup>[a]</sup> Zhifang Guo,<sup>[a]</sup> Glen B. Deacon,<sup>[b]</sup> and Peter C. Junk<sup>\*[a]</sup>

The preparation and characterization of six rare earth 2-methyl-3-furoate (2m3fur) complexes are detailed in this study. Analysis through single-crystal X-ray diffraction, as well as powder XRD, reveals that all six compounds belong to one of two structural groups:  $\{[RE_2(2m3fur)_6(EtOH)] \cdot H_2O\}_n$  (RE = La, Ce, Pr) and  $[RE_3(2m3fur)_9]_n$  (RE = Y, Er, Yb). These structural groups feature carboxylate coordinated linear polymers. The former complexes have two distinct metal centers, one ten coordinate and one nine, with lattice water participating in a hydrogen bond with

coordinated ethanol. The latter structures, involving erbium, ytterbium, and yttrium, have three unique metal centers: two eight coordinate, and one seven-coordinated. In corrosion inhibition tests on mild steel in 0.01 M NaCl solution, the maximum efficiency was observed with  $[Y_3(2m3fur)_9]_n$  at 59%, which is less effective than yttrium 3-furoate (90% efficiency). The results suggest that the steric effect of the methyl group adversely affects corrosion inhibition.

## 1. Introduction

Rare earth carboxylates constitute the largest class of rare earth-based coordination polymers,<sup>[1]</sup> showcasing diverse structural types and coordination modes.<sup>[2–5]</sup> These complexes are known for their high coordination numbers, achieved through the favourable large size and high charge of lanthanoid ions, the multiplicity of carboxylate binding modes, and the lack of directionality in lanthanoid-carboxylate binding.<sup>[2]</sup>

Over the past two decades, the combination of the properties of rare earth ions and aromatic carboxylates has given rise to the development of highly effective dual-function rare earth carboxylate corrosion inhibitors. These compounds have emerged as a promising and greener alternative to toxic chromates in the field of corrosion prevention.<sup>[1,6–10]</sup> Some of the best-performing compounds include cerium salicylate<sup>[8]</sup> lanthanum 4-hydroxycinnamate<sup>[11]</sup> and yttrium 3-(4'-methylbenzoyl)propionate<sup>[12]</sup> 3-furoate<sup>[13]</sup> and 4-hydroxybenzoate.<sup>[14]</sup> Emerging trends suggest that additional unsaturation, donor capacity, and the presence of donor hetero atoms play a significant role in achieving higher levels of inhibition.<sup>[8,9,12,13,15,16]</sup> Such observations support an inhibition model whereby a carboxylatolanthanoid species binds to a

hydroxidoiron(III) group on a corroding surface through a donor group-hydroxide interaction.<sup>[8–10]</sup>

To examine this concept further, we have utilised our recent discovery of the high inhibitor activity of lanthanoid 3-furoate complexes.<sup>[13]</sup> Accordingly, we have introduced a 2-methyl group into the 3-furoate ion and examined the effect of its steric inhibition on carboxylate coordination and capacity for corrosion inhibition. Six lanthanoid complexes of 2-methyl-3-furoate have been prepared, their structures examined by X-ray crystallography, X-ray powder diffraction, and thermogravimetric analysis, and corrosion testing outcomes based on weight loss measurements determined. The structural change has a deleterious effect on inhibitor activity.

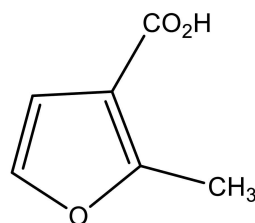


Chart 1. Structure of 2-methyl-3-furoic acid (2m3furH).

## 2. Results and Discussion

### 2.1. Synthesis and Characterization

The complexes  $\{[RE_2(2m3fur)_6(EtOH)] \cdot H_2O\}_n$  (**1RE** = La, Ce, Pr) and  $[RE_3(2m3fur)_9]_n$  (**2RE** = Y, Er, Yb) were prepared in moderate yields by using metathesis reactions between sodium 2-methyl-3-furoate and the corresponding RE salts (at a mole ratio of 3:1) as shown in Scheme 1.

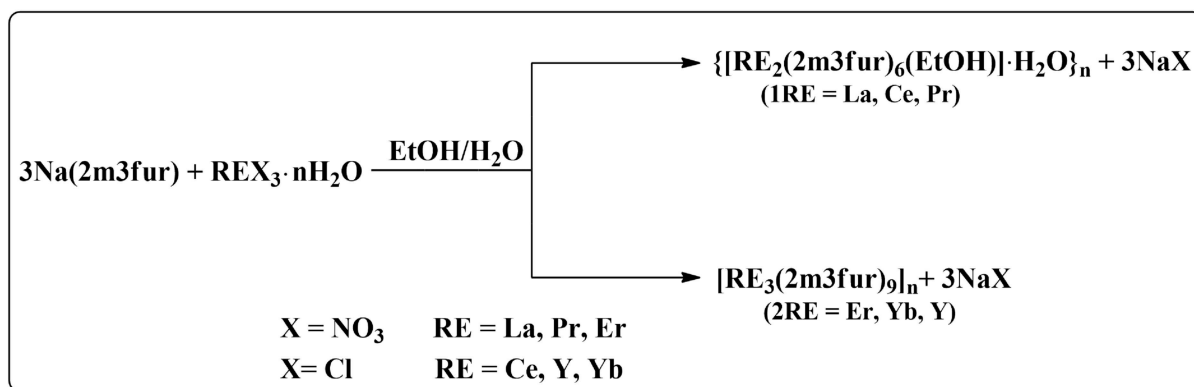
The compositions of all these complexes were determined through a combination of X-ray crystallography, elemental analysis and TGA. Growing crystals for X-ray diffraction proved

[a] V. P. Vithana, Z. Guo, P. C. Junk  
College of Science & Engineering, James Cook University, Townsville, 4811,  
Qld, Australia  
E-mail: peter.junk@jcu.edu.au

[b] G. B. Deacon  
School of Chemistry, Monash University, Clayton, 3800, Vic., Australia

Supporting information for this article is available on the WWW under  
<https://doi.org/10.1002/ejic.202300722>

© 2024 The Authors. European Journal of Inorganic Chemistry published by Wiley-VCH GmbH. This is an open access article under the terms of the Creative Commons Attribution Non-Commercial NoDerivs License, which permits use and distribution in any medium, provided the original work is properly cited, the use is non-commercial and no modifications or adaptations are made.



Scheme 1. The synthesis of RE 2-methyl-3-furoate complexes.

Compound	$\nu(\text{OH})_{\text{water}}$	$\nu_{\text{as}}(\text{CO}_2^-)$	$\nu_{\text{s}}(\text{CO}_2^-)$	$\Delta\nu = (\nu_{\text{as}} - \nu_{\text{s}})_{\text{avg}}$	$\delta(\text{CO}_2)$
$\{[\text{Ce}_2(2\text{m3fur})_6(\text{EtOH})] \cdot \text{H}_2\text{O}\}_n$ (1b)	3458	1518	1377, 1360	149.5	684
$[\text{Er}_3(2\text{m3fur})_9]_n$ (2b)	–	1531, 1517	1381, 1360	153.5	686

to be particularly challenging when using the 2-methyl-3-furoate ligand. However, in this study, we successfully obtained single crystals suitable for X-ray crystallography for **1c**, **2a**, **2b** and **2c**. In each instance, the bulk products were isolated as powders.

All attempts to obtain crystals of **1a** were unsuccessful. Nevertheless, X-ray powder diffractograms suggest it is isomorphous with **1c** (Figure S1). Data for **1b** were incomplete, resulting in the acquisition of only the unit cell. However, the unit cell parameters and the powder diffractogram of this complex indicate that it is isomorphous with **1c**.

TGA analyses of compound **1a** and **1b** yielded results consistent with the crystal composition of  $\{[\text{RE}_2(2\text{m3fur})_6(\text{EtOH})] \cdot \text{H}_2\text{O}\}_n$ , indicating the simultaneous loss of one water molecule and one ethanol molecule in a single step. The presence of a broad band in the range 3200–3550 cm<sup>-1</sup> in the IR spectra of **1a** and **1b** is consistent with the presence of water and ethanol (O–H stretching) in the compounds. The elemental analysis data indicate that complexes **1a** and **1b** experienced ethanol loss from their single crystal compositions under the microanalysis drying conditions. As for compound **1c**, elemental analysis, TGA and IR indicate that, during the drying process, both coordinated ethanol and lattice water were removed from the crystals (Figure S2 and S3).

For compounds **2a**, **2b**, and **2c**, the powder XRD analyses closely resembled the patterns generated from the single-crystal data (see Figure S4). Consistent with the single-crystal compositions of compounds **2a** and **2b**, their thermograms and IR spectra do not exhibit any weight reduction attributable to the removal of coordinated or lattice solvent molecules (Figure S5 and Figure S6). Conversely, **2c** displayed hygroscopic properties, evident from the thermal analysis. Thus, TGA data for **2c** revealed additional water content, with the loss of four

water molecules occurring in a single step below 150 °C (Figure S6). Nevertheless, the IR spectrum, recorded after drying to a constant weight, did not exhibit a broad band in the range 3200–3550 cm<sup>-1</sup> (Figure S5), and the elemental analyses of **2a**–**2c** were consistent with anhydrous compounds.

The infrared spectra of all complexes exhibited distinctive peaks within the range of 1560–1360 cm<sup>-1</sup> corresponding to carboxylate COO<sup>-</sup> stretching bands. The IR spectra of the compounds exhibit strong similarities in major bands within each isostructural series. Therefore, we have listed the significant IR bands for only one compound from each series, specifically **1b** and **2b**, in Table 1.

## 2.2. Structural Description

There are only two distinct carboxylate ligand binding modes in the structures, namely bridging tridentate  $\mu\text{-}1\kappa(\text{O}, \text{O}')\text{:}2\kappa(\text{O}')$  and *syn-syn* bridging bidentate  $\mu\text{-}1\kappa(\text{O})\text{:}2\kappa(\text{O}')$  (Figure 1). In comparison, analogous 3fur complexes display four unique binding

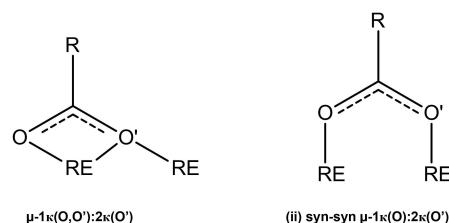


Figure 1. Coordination forms of 2-methyl-3-furoate ions in rare earth complexes. PLEASE ENSURE *syn-syn* are in italics in caption for (ii) and add (i) under the first compound

modes: *syn-syn*  $\mu$ -1 $\kappa$ (O):2 $\kappa$ (O'), *syn-anti*  $\mu$ -1 $\kappa$ (O):2 $\kappa$ (O'),  $\mu_3$ -1 $\kappa$ (O):2 $\kappa$ (O,O'):3 $\kappa$ (O') and  $\mu_3$ -1 $\kappa$ (O):2 $\kappa$ (O'):3 $\kappa$ (O').<sup>[13]</sup>

Due to poor quality of crystals of **2b** ( $R_{\text{int}}$  19.96%), compound **2b** is presented for connectivity purposes only. However, **2b** is isomorphous with **2a** and **2c**.

### 2.2.1. 1D polymeric chains of $\{[\text{RE}_2(2\text{m3fur})_6(\text{EtOH})] \cdot \text{H}_2\text{O}\}_n$ complexes (RE = La, Ce, Pr)

The molecular structure of  $\{[\text{Pr}_2(2\text{m3fur})_6(\text{EtOH})] \cdot \text{H}_2\text{O}\}_n$  (**1c**) is depicted in Figure 2 and serves as a representative of the isomorphous series of 1D polymeric complexes,  $\{[\text{RE}_2(2\text{m3fur})_6(\text{EtOH})] \cdot \text{H}_2\text{O}\}_n$  (RE = La (**1a**), Ce (**1b**) and Pr (**1c**)). The structure of  $\{[\text{Pr}_2(2\text{m3fur})_6(\text{EtOH})] \cdot \text{H}_2\text{O}\}_n$  is binuclear, crystal-

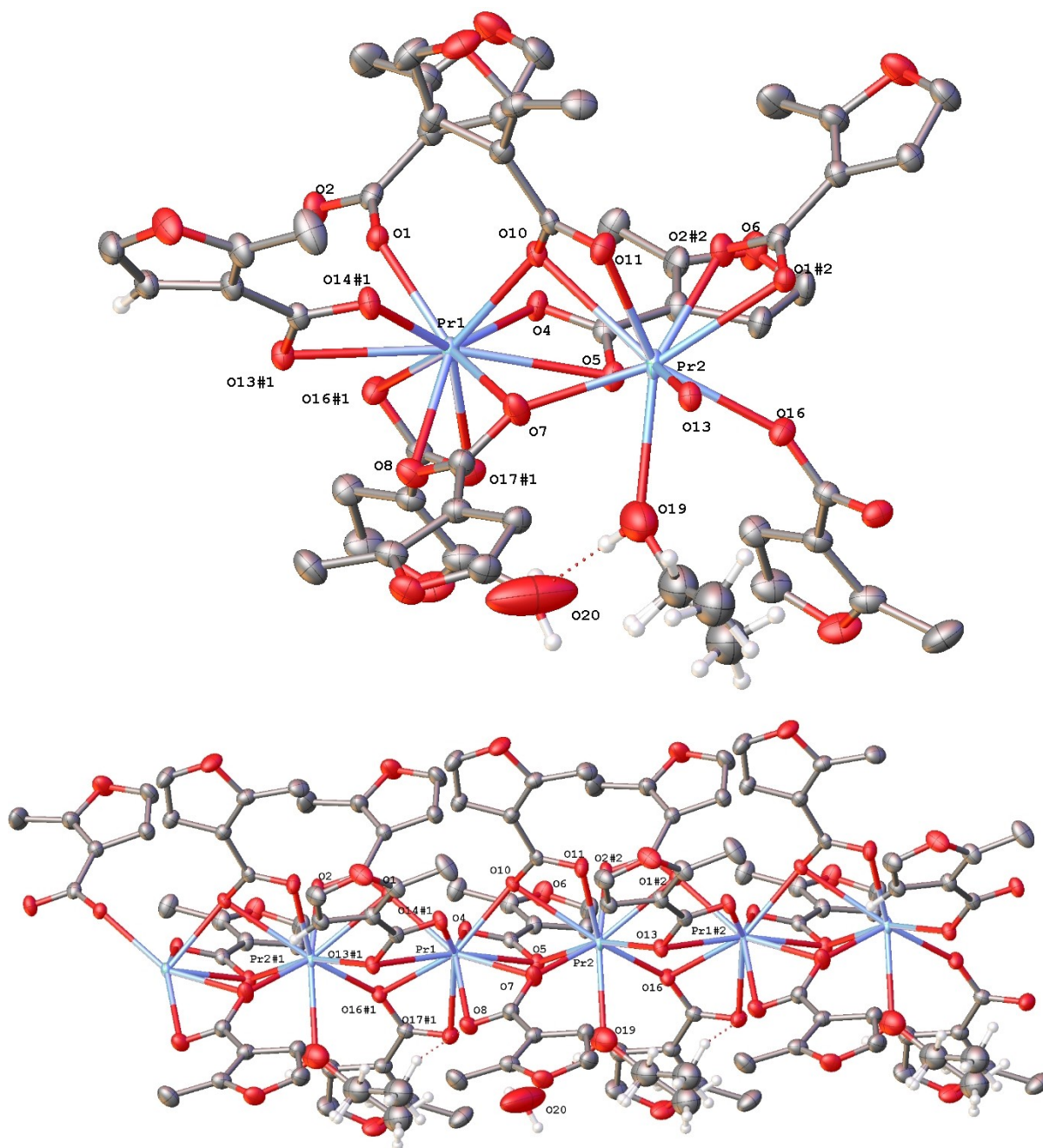


**Figure 2.** (a) The immediate coordination environment around Pr metal atoms in  $\{[\text{Pr}_2(2\text{m3fur})_6(\text{EtOH})] \cdot \text{H}_2\text{O}\}_n$  (**1c**); (b) 1D polymeric chain of **1c** (representative of **1a**, **1b**) Selected bond lengths (Å) and angles (°) (Complete data set for **1c** is in the supplementary information; Table S2 and Table S3). 1c Pr1-O1 2.401(2), Pr1-O4 2.456(3), Pr1-O5 2.779(3), Pr1-O7 2.603(3), Pr1-O8 2.529(3), Pr1-O10 2.411(2), Pr1-O13#1 2.830(3), Pr1-O14#1 2.464(3), Pr1-O16#1 2.604(2), Pr1-O17#1 2.558(3), Pr2-O5 2.396(3), Pr2-O7 2.428(3), Pr2-O10 2.768(2), Pr2-O11 2.434(3), Pr2-O13 2.391(3), Pr2-O16 2.436(3), Pr2-O19 2.619(4), Pr2-O1#2 2.716(2), Pr2-O2#2 2.451(3), Pr1...Pr2 3.8477(8), Pr2...Pr1#2 3.8433(8), Pr2#1-Pr1-Pr2 177.360(9), Pr1-Pr2-Pr1#2 177.360(9), Pr1-O5-Pr2 95.78(8), Pr1-O7-Pr2 99.73(9), Pr1-O10-Pr2 95.70(3), Symmetry Code: #1 +X, +Y, +Z; #2 -1 +X, +Y, +Z.

lizing in the monoclinic  $P2_1/c$  space group, containing two distinct  $\text{Pr}^{+3}$  metal centers within the asymmetric unit. There only one carboxylate binding mode, resulting in a distorted bicapped square antiprism (SAP)-type deca coordination for Pr1 and a distorted tricapped trigonal prism-type nine coordination for Pr2. Crystal refinement data and bond lengths of **1c** are provided in the supplementary material (Table S1 and S2).

The coordination sphere around the Pr1 metal center comprises eight chelating oxygen atoms from four  $\mu\text{-}1\kappa(\text{O},\text{O}')\text{:}2\kappa(\text{O}')$  carboxylates (O4,5), (O7,8), (O13#1,14#1), (O16#1,17#1) and two bridging oxygen atoms from  $\mu\text{-}1\kappa(\text{O})\text{:}2\kappa(\text{O},\text{O}')$  carboxylates (O1, O10). The Pr2 metal center is nine coordinate, featuring four chelating oxygen atoms from two  $\mu\text{-}1\kappa(\text{O},\text{O}')\text{:}2\kappa(\text{O}')$  carboxylates (O10,11), (O1#2,2#2), four bridging oxygen atoms from  $\mu\text{-}1\kappa(\text{O})\text{:}2\kappa(\text{O},\text{O}')$  carboxylates (O5, O7, O13, O16), and one oxygen atom (O19) from the ligated ethanol.

The two metal centres are connected by three ligands (through O5, O7, O10), forming a 1D polymeric chain and this chain propagates in an alternating sequence of Pr2#1...Pr1...Pr2...Pr1#2. The metal-metal distance between Pr1...Pr2 and Pr2...Pr1#2 are 3.8477(8) Å and 3.8433(8) Å respectively, with Pr2#1-Pr1-Pr2 and Pr1-Pr2-Pr1#2 angles of 177.360(9)°. The angles formed at the bridging oxygen atoms are 95.78(8)° (Pr1-O5-Pr2), 99.73(9)° (Pr1-O7-Pr2) and 95.70(3)° (Pr1-O10-Pr2).

Additionally, the lattice water oxygen atom (O20) forms a hydrogen bond with the oxygen atom (O19) of the ligated ethanol molecule within the asymmetric unit. The experimentally observed hydrogen bonding interactions are listed in Table S4.

At first sight, the higher coordination numbers (10, 9) in **1a-c** than in RE 3-furoate (3fur) complexes,  $[\text{RE}(\text{3fur})_3(\text{H}_2\text{O})_2]_n$  (RE = La–Ho, Y), which are eight coordinate, is counter intuitive given the greater bulk of 2m3fur. However, the higher coordination numbers are associated with longer RE–O bonds relieving strain about the metal center (Table 2). The simpler carboxylate coordination in **1a-c** than in the 3fur analogues may be attributable to reduced access to one of the carboxylate oxygens owing the bulk of the Me group. Any electronic effect of the methyl group is outweighed by the steric effect as shown by the considerable simplification of the carboxylate coordination compared with that in lanthanoid 3-furoates.

### 2.2.2. 1D polymeric chains of $[\text{RE}_3(\text{2m3fur})_9]_n$ complexes (RE = Y, Er, Yb)

The asymmetric unit of the isostructural series of complexes  $[\text{RE}_3(\text{2m3fur})_9]_n$  (RE = Y (**2a**), Er (**2b**) and Yb (**2c**)) comprises three unique RE metal centers, forming a 1D polymeric chain.

Table 2. Average RE–O bond length comparison of Pr 3-furoate and Pr 2-methyl-3-furoate complexes		
	RE1–O	RE2–O
$[\text{Pr}(\text{3fur})_3(\text{H}_2\text{O})_2]_n^{[13]}$	2.43	
$\{[\text{Pr}_2(\text{2m3fur})_6(\text{EtOH})] \cdot \text{H}_2\text{O}\}_n$	2.56	2.53

They crystallize in the  $P2_1/c$  space group. Crystal data and specific refinement parameters are provided in the supplementary material. A representative structure,  $[\text{Yb}_3(\text{2m3fur})_9]_n$  is shown in Figure 3.

Yb1 and Yb3 are both octa-coordinate and Yb2 seven coordinate. The arrangement around the Yb1 metal center is distorted square antiprismatic, whereas a distorted dodecahedral arrangement can be seen around Yb3. Each Yb ion is coordinated by chelating oxygen atoms from two  $\mu\text{-}1\kappa(\text{O},\text{O}')\text{:}2\kappa(\text{O}')$  carboxylates. Specifically, Yb1 is bound by (O15,16) and (O22#2,23#2), whereas Yb3 is coordinated by (O20,21) and (O11#1,12#1). In the case of Yb1, three additional coordination sites are occupied by carboxylate oxygen atoms (O4, O5, O14) originating from  $\mu\text{-}1\kappa(\text{O})\text{:}2\kappa(\text{O}')$  bridging ligands. Conversely, Yb3 possesses only two such bridging oxygen atoms (O3#1,25) surrounding it. The final coordination oxygen atom (O12) of Yb1 is derived from a  $\mu\text{-}1\kappa(\text{O})\text{:}2\kappa(\text{O},\text{O}')$  bridge, while two of these bridging oxygen atoms (O18, 22) complete the coordination sphere around Yb3.

The stereochemistry of the seven coordinated Yb2 is pentagonal bipyramidal, and it is coordinated by two oxygen atoms (O17,18) from a  $\mu\text{-}1\kappa(\text{O},\text{O}')\text{:}2\kappa(\text{O}')$  chelating carboxylate, two oxygen atoms (O16, O20) from  $\mu\text{-}1\kappa(\text{O})\text{:}2\kappa(\text{O},\text{O}')$  bridging carboxylate ligands, and three bridging oxygen atoms (O7, O19, O24) from  $\mu\text{-}1\kappa(\text{O})\text{:}2\kappa(\text{O}')$  carboxylate groups.

The one-dimensional polymeric chain of **2c** exhibits a slight wave, with angles of 157.006(12)°, 160.657(10)°, and 148.256(15)° between Yb1–Yb2–Yb3, Yb2–Yb3–Yb1#1 and Yb#2–Yb1–Yb2, respectively.

Table S5 presents the list of Yb–O bond lengths observed in the crystal structure. The overall average Yb–O bond distance is 2.32 Å, with Yb3–O12#1 being the longest and Yb2–O7 the shortest. The average bond lengths around each Yb metal center are as follows: Yb1 (2.33 Å), Yb2 (2.29 Å), Yb3 (2.34 Å). There is an increase of approximately 0.04 Å in the average Yb–O bond length at Yb1 and Yb3 metal centers compared to the Yb2 metal center, a result which correlates with the increasing coordination number of  $\text{Yb}^{3+}$ .

The separation between each pair of Yb metal centers is as follows: Yb1...Yb2 (4.1275(9) Å), Yb2...Yb3 (3.8100(9) Å) and Yb3...Yb1#1 (3.7230(8) Å). Yb1...Yb2 is bridged by three oxygen atoms from one  $\mu\text{-}1\kappa(\text{O})\text{:}2\kappa(\text{O},\text{O}')$  bridge and two  $\mu\text{-}1\kappa(\text{O})\text{:}2\kappa(\text{O}')$  bridges, while Yb2...Yb3 and Yb3...Yb1#1 are each bridged by oxygen atoms from two  $\mu\text{-}1\kappa(\text{O})\text{:}2\kappa(\text{O},\text{O}')$  bridges and one  $\mu\text{-}1\kappa(\text{O})\text{:}2\kappa(\text{O}')$  bridge. The impact of the lanthanoid contraction<sup>[17]</sup> is evident in the decreased RE–O bond distances within the 1D chains of  $\text{Y}^{3+}$ ,  $\text{Er}^{3+}$  and  $\text{Yb}^{3+}$  complexes (Table S5).

As two of the Y atoms of **2a** have the same coordination number as in  $[\text{Y}(\text{3fur})_3(\text{H}_2\text{O})_2]_n$ , it is possible to compare  $\langle \text{Y–O} \rangle$  values (Table 3), and they suggest a slight lengthening in **2a**, consistent with a steric effect by the methyl group. Any electronic effect of the methyl group is outweighed by the steric effect as shown by the considerable simplification of the carboxylate coordination compared with that in lanthanoid 3-furoates, and by Y–O bond lengthening in **2a**.



**Table 4.** Observed weight loss, corrosion rates ( $\mu\text{g}/\text{m}^2\text{s}$ ) and percentage inhibition ( $\eta$ ) for mild steel coupons immersed in specific solutions at 800 ppm concentrations in 0.01 M NaCl for seven days.

Solution	Concentration		Solubility in 0.01 M NaCl (ppm)	Avg Weight Loss (mg)	Corrosion Rate ( $\mu\text{g}/\text{m}^2\text{s}$ )	Inhibition, $\eta$ (%)
	ppm	mM				
Control - NaCl	580	10	–	19.6	39.1	–
$\{[\text{Ce}_2(2\text{m3fur})_6(\text{EtOH})] \cdot \text{H}_2\text{O}\}_n$ <b>1 b</b>	800	0.731	1800	12.6	24.0	39
$\{[\text{Pr}_2(2\text{m3fur})_6(\text{EtOH})] \cdot \text{H}_2\text{O}\}_n$ <b>1 c</b>	800	0.730	1500	8.8	20.9	46
$[\text{Y}_3(2\text{m3fur})_9]_n$ <b>2 a</b>	800	0.574	850	8.5	16.2	59
$[\text{Er}_3(2\text{m3fur})_9]_n$ <b>2 b</b>	800	0.491	800	11.3	21.6	45
$[\text{Yb}_3(2\text{m3fur})_9]_n$ <b>2 c</b>	800	0.486	830	9.7	18.5	53
$[\text{Ce}(3\text{fur})_3(\text{H}_2\text{O})_2]_n$ <sup>[13]</sup>	800	1.57	3000	3.7	8.3	79
$[\text{Y}(3\text{fur})_3(\text{H}_2\text{O})_2]_n$ <sup>[13]</sup>	800	1.75	800	1.9	3.9	90

$$\text{Corrosion rate (R)} = \frac{KW}{ATD} \quad (1)$$

Subsequently, the percentage corrosion inhibition (%) was calculated using Equation (2):

$$\eta = \frac{R(\text{Control}) - R(\text{inhibitor})}{R(\text{Control})} \times 100 \quad (2)$$

Consistent with visual inspections (Figure S7), weight loss measurements also indicated that  $[\text{Y}_3(2\text{m3fur})_9]_n$  **2 a** exhibited the highest inhibition efficiency at 59% among the tested compounds, while  $\{[\text{Ce}_2(2\text{m3fur})_6(\text{EtOH})] \cdot \text{H}_2\text{O}\}_n$  **1 b** showed the lowest performance with an inhibition efficiency of approximately 39%.

The limited solubility of most of the complexes hindered attempts to conduct studies at higher concentration. The performance of the RE 2-methyl-3-furoate complexes was not as effective as the analogous rare earth 3-furoate complexes (see Table 4 for a comparison of Ce and Y complexes),<sup>[13]</sup> suggesting that the methyl substituent on the furoate ring may cause steric hindrance of inhibitor function. Because of the less effective inhibitor performance, electrochemical assessments of inhibition were not pursued.

### 3. Conclusions

Two series of RE 2-methyl-3-furoate complexes,  $\{[\text{RE}_2(2\text{m3fur})_6(\text{EtOH})] \cdot \text{H}_2\text{O}\}_n$  **1RE** (RE = La, Ce, Pr) and  $[\text{RE}_3(2\text{m3fur})_9]_n$  **2RE** (RE = Y, Er, Yb) have been successfully synthesized. These compounds crystallized in one of the two distinct structural groups, as determined through single-crystal X-ray crystallography. The synthesis process yielded moderate isolated yields of crystalline materials, and these complexes were comprehensively characterized by various techniques, including IR spectroscopy, powder XRD, TGA, and microanalyses.

The light rare earth metals form one-dimensional polymeric structures,  $\{[\text{RE}_2(2\text{m3fur})_6(\text{EtOH})] \cdot \text{H}_2\text{O}\}_n$  complexes (RE = La, Ce, Pr) with one ten and one nine coordinate RE atom. Conversely,

the heavier rare earth metals have one-dimensional polymeric chains in the  $[\text{RE}_3(2\text{m3fur})_9]_n$  complexes (RE = Y, Er, Yb), with three unique RE metal centers, two eight coordinate and one seven coordinate.

In immersion studies conducted with mild steel in 0.01 M NaCl solutions at inhibitor concentrations of 800 ppm,  $[\text{Y}_3(2\text{m3fur})_9]_n$  **2 c** emerged as the most effective inhibitor among the compounds tested, demonstrating a 59% inhibition rate. Nevertheless, the most efficient inhibitor in this study proved to be less effective than the RE 3-thiophenecarboxylate<sup>[16]</sup> and 3-furoate<sup>[13]</sup> complexes studied previously. It is plausible that the steric effect of the methyl substituent impedes binding of the inhibitor to OH groups on the corroded steel surface, thereby reducing inhibitor protection.

## Materials and Methods

### General Considerations

All reagents and solvents used were of standard commercial grade and were employed without further purification. IR data were obtained in the region 4000–500  $\text{cm}^{-1}$  by using a Nicolet™ iS™ 5 FTIR Spectrometer. Elemental analyses (C, H) were performed by the Microanalytical Laboratory at the Science Centre, London Metropolitan University, England. Metal analyses were conducted through complexometric titration with 0.01 M EDTA, Xylenol Orange indicator and hexamethylenetetramine buffer. Thermogravimetric analysis (TGA) was carried out using a TA instrument SDT 650 with standard 90  $\mu\text{l}$  alumina metal pans under a  $\text{N}_2$  atmosphere (at a flow rate of 50  $\text{ml min}^{-1}$ ), ranging from room temperature up to 750  $^\circ\text{C}$  (with a ramp of 10  $^\circ\text{C min}^{-1}$ ) (Figure S2 and S6). Melting points were determined in glass capillaries and are reported without calibration. Powder XRD measurements were obtained at room temperature using a Bruker D2 PHASER diffractometer in the range of 5–50 $^\circ$  with a 0.2 $^\circ$  divergence slit and at 0.02 $^\circ$  increments. X-ray powder simulations were generated using the Mercury program provided by the Cambridge Crystallographic Data Centre,<sup>[18]</sup> based on the obtained single-crystal X-ray diffraction data.

## X-ray Crystallography

Single crystals of all samples were coated in viscous hydrocarbon oil and mounted on glass fibres or loops on the diffractometer. The data were collected on the MX1 beamline at the Australian Synchrotron, where the data integration was processed with Blueice<sup>[19]</sup> and XDS<sup>[20]</sup> software programs. Structures were solved by SHELXT and refined by full-matrix least-squares methods against  $F^2$  using SHELXL2018,<sup>[21]</sup> within the Olex2<sup>[22]</sup> interface. All hydrogen atoms were placed in calculated positions using the riding model. Crystal data and refinement details are shown in Table S1. CCDC 2308961 for **1c** and 2308962–2308964 for compounds **2a–2c**, contain the supplementary crystallographic data for this paper. These data can be obtained free of charge from The Cambridge Crystallographic Data Centre.

## Synthesis of 2-methyl-3-furoate (2m3fur) RE complexes

General Synthetic Method: 2-Methyl-3-furoic acid was dissolved in 95% ethanol (15 ml) and subjected to deprotonation by an equimolar quantity of aqueous sodium hydroxide. The solution mixture was stirred for one hour, after which the pH was adjusted to fall within the range 7–8. Subsequently, three molar equivalents of sodium 2-methyl-3-furoate were treated with one molar equivalent of the hydrated rare earth salt solution at a pH level of 5 to form rare earth 2-methyl-3-furoate complexes. The resulting solid precipitates were isolated by filtration and allowed to air-dry for 2–3 days. Finally, crystals were obtained through slow evaporation of the mother liquor at room temperature.

**1a:**  $\{[La_2(2m3fur)_6(EtOH)] \cdot H_2O\}_n$  white powder. Yield: 52%. m.p. 230 °C (dec). Elemental analysis calculated for  $C_{38}H_{38}La_2O_{20}$  (MW: 1092.51  $gmol^{-1}$ ): Calculated (%) C 41.78; H 3.51; La 25.40;  $C_{36}H_{32}La_2O_{19}$  (MW: 1046.44  $gmol^{-1}$ , loss of 1 EtOH): Calculated (%) C 41.32; H 3.08; La 26.55; Found (%) C 41.39; H 2.62; La 26.65. IR ( $cm^{-1}$ ): 3430w, 3123w, 2920w, 1682w, 1595 m, 1530s, 1519 s, 1445 m, 1414 s, 1376 s, 1359 s, 1232 m, 1213 s, 1134 m, 1101 s, 1033w, 946 m, 896 m, 875w, 817 s, 807 s, 731 s, 684 m, 634w, 599 m, 534 m, 462 s. TGA weight loss (30–200 °C); 4.9% (Calc. for loss of  $1 \times H_2O$  and  $1 \times EtOH = 5.8\%$ ).

**1b:**  $\{[Ce_2(2m3fur)_6(EtOH)] \cdot H_2O\}_n$  white powder. Yield: 52%. m.p. 230 °C (dec). Elemental analysis for  $C_{38}H_{38}Ce_2O_{20}$  (MW: 1094.93  $gmol^{-1}$ ): Calculated (%) C 41.68; H 3.50; Ce 25.60;  $C_{36}H_{32}Ce_2O_{19}$  (MW: 1048.86  $gmol^{-1}$ , loss of 1 EtOH): Calculated (%) C 41.22; H 3.08; Ce 26.72; Found (%) C 41.55; H 2.54; Ce 27.26. IR ( $cm^{-1}$ ): 3458w, 3122w, 2922w, 1596 m, 1527 s, 1518 s, 1444 m, 1414 s, 1376 s, 1359 s, 1232 m, 1214 s, 1133 m, 1102 s, 1031w, 946 m, 895 m, 876w, 819 s, 807 s, 733 s, 684 m, 634w, 600 m, 534 m, 466 s, 457 s. TGA weight loss (30–175 °C); 4.8% (Calc. for loss of  $1 \times H_2O$  and  $1 \times EtOH = 5.8\%$ ); Monoclinic  $P2_1/n$ , unit Cell:  $a = 7.6700(15)$ ,  $b = 22.470(4)$ ,  $c = 23.620(5)$ ,  $\beta = 98.85(3)$ , which is similar to **1c**.

**1c:**  $\{[Pr_2(2m3fur)_6(EtOH)] \cdot H_2O\}_n$  pale green powder. Yield: 48%. m.p. 230 °C (dec). Elemental analysis for  $C_{38}H_{38}O_{20}Pr_2$  (MW: 1096.51  $gmol^{-1}$ ): Calculated (%) C 41.62; H 3.49; Pr 25.70;  $C_{36}H_{30}O_{18}Pr_2$  (MW: 1032.43  $gmol^{-1}$ , loss of 1 EtOH and 1  $H_2O$ ): Calculated (%) C 41.88; H 2.93; La 27.30; Found (%) C 41.70; H 2.50; Pr 27.95; IR ( $cm^{-1}$ ): 3122w, 2923w, 1596 m, 1548 s, 1534 m, 1515 s, 1412 s, 1375 s, 1358 s, 1235 m, 1214 s, 1133 m, 1102 s, 1030w, 946 m, 895 m, 876w, 836w, 821 s, 806 s, 737 s, 726 s, 685 m, 634w, 600 m, 535 m, 466 s, 458 s.

**2a:**  $[Y_3(2m3fur)_9]_n$  white powder. Yield: 73%. m.p. 270 °C (dec). Elemental analysis for  $C_{54}H_{45}O_{27}Y_3$  (MW: 1392.63  $gmol^{-1}$ ): Calculated (%) C 46.57; H 3.26; Y 19.20; Found (%) C 46.64; H 2.92; Y 19.60. IR ( $cm^{-1}$ ): 3127w, 2922w, 1596 m, 1532 s, 1517 s, 1462 s, 1445 m, 1420s, 1381 m, 1360s, 1233 m, 1217 s, 1132 m, 1103 m, 1030w,

946 m, 895 m, 837 m, 802 s, 750 m, 728 s, 685 m, 600 m, 553w, 534w, 473 s.

**2b:**  $[Er_3(2m3fur)_9]_n$  pink powder. Yield: 70%. m.p. 270 °C (dec). Elemental analysis for  $C_{54}H_{45}O_{27}Er_3$  (MW: 1627.69  $gmol^{-1}$ ): Calculated C 39.85; H 2.79; Er 30.80; Found (%) C 39.80; H 2.58; Er 31.32. IR ( $cm^{-1}$ ): 3127w, 1596 m, 1531 s, 1517 s, 1463 m, 1444 s, 1420s, 1381 m, 1360s, 1233 m, 1217 s, 1131 m, 1103 s, 1030w, 947 m, 895 m, 837 m, 802 s, 751w, 728 s, 688 m, 600 m, 553 m, 534w, 472 s.

**2c:**  $[Yb_3(2m3fur)_9]_n$  white powder. Yield: 55%. m.p. 270 °C (dec). Elemental analysis for  $C_{54}H_{45}O_{27}Yb_3$  (MW: 1645.04  $gmol^{-1}$ ): Calculated (%) C 39.43; H 2.76; Yb 31.60; Found (%) C 39.55; H 2.50; Yb 31.70. IR ( $cm^{-1}$ ): 3129w, 2923w, 1599 m, 1538 m, 1513 s, 1460s, 1428 s, 1385 m, 1361 s, 1220s, 1130 m, 1107 m, 1030w, 945 m, 896 m, 840 m, 805 s, 729 s, 684 m, 634w, 600 m, 562 m, 536w, 469 s. TGA weight loss (90–175 °C); 4.4% (Calc. for loss of  $4 \times H_2O$  (Assuming absorb water = 4.2%)).

## Corrosion Testing

Weight loss experiments were carried out in accordance with the established ASTM G31-72 protocol<sup>[23]</sup> to evaluate the overall corrosion and inhibition characteristics of the synthesized compounds. For the weight loss tests, coupons made from AS 1020 mild steel alloy were prepared. These coupons were cut to dimensions of approximately  $20 \times 20 \times 1.5$  mm and subsequently subjected to gradual abrasion using sanding sheets with grit sizes ranging from 80 to 2000. Afterward, the samples were cleaned with distilled water and then ethanol, and they were dried using nitrogen gas. These coupons were immediately used for immersion tests, lasting up to 168 hours (7 days). Both the test samples and the control coupons were immersed in separate beakers filled with 0.01 M NaCl solutions, with and without the addition of 800 ppm of the inhibitor compounds. In each arrangement, replicates were carried out by completely immersing the coupons at a mid-depth level, using teflon strings.

After completing the test, the first step involved gently removing any corrosion product adhering to the substrate through mild sonication in clean distilled water. Subsequently, the finest sanding papers were used with minimal force to prevent the removal of the sound material. Finally, the coupons were rinsed with ethanol and dried using nitrogen ( $N_2$ ) gas.

## Acknowledgements

PCJ and GBD gratefully acknowledge the ARC for funding (DP200100568). Parts of this research were undertaken on the MX1 beamline at the Australian Synchrotron, part of ANSTO.<sup>[24]</sup> Open Access publishing facilitated by James Cook University, as part of the Wiley - James Cook University agreement via the Council of Australian University Librarians.

## Conflict of Interests

The authors declare no conflict of interest.

## Data Availability Statement

The data that support the findings of this study are available from the corresponding author upon reasonable request.

**Keywords:** rare earth metal · carboxylate complexes · metathesis · 2-methyl-3-furoates · corrosion inhibitors

- [1] T. Behrsing, G. B. Deacon and P. C. Junk, in *Rare Earth-Based Corrosion Inhibitors*, (Eds. M. Forsyth B. Hinton), Woodhead Publishing, Cambridge, **2014**, pp. 1–37.
- [2] N. C. Thomas, O. A. Beaumont, G. B. Deacon, C. Gaertner, C. M. Forsyth, A. E. Somers, P. C. Junk, *Aust J Chem* **2020**, *73*, 1250–1259.
- [3] A. Ouchi, Y. Suzuki, Y. Ohki, Y. Koizumi, *Coord. Chem. Rev.* **1988**, *92*, 29–43.
- [4] C.-H. Huang, *Rare earth coordination chemistry: fundamentals and applications*, John Wiley & Sons, **2010**, p. 592.
- [5] R. Janicki, A. Mondry, P. Starynowicz, *Coord Chem Rev* **2017**, *340*, 98–133.
- [6] B. Hinton, in *Handbook on the Physics and Chemistry of Rare Earths*, (Eds. K. A. Gschneidner, L. Eyring) Elsevier Science B. V., **1995**, vol. 21, pp. 29–92.
- [7] J. Sinko, *Prog. Org. Coat.* **2001**, *42*, 267–282.
- [8] M. Forsyth, M. Seter, B. Hinton, G. Deacon, P. Junk, *Aust. J. Chem.* **2011**, *64*, 812–819.
- [9] A. E. Somers, G. B. Deacon, B. R. W. Hinton, D. R. Macfarlane, P. C. Junk, M. Y. J. Tan, M. Forsyth, *J. Indian Inst. Sci.* **2016**, *96*, 285–292.
- [10] A. E. Somers, Y. Peng, A. L. Chong, M. Forsyth, D. R. MacFarlane, G. B. Deacon, A. E. Hughes, B. R. W. Hinton, J. I. Mardel, P. C. Junk, *Corros. Eng., Sci. Technol.* **2020**, *55*, 311–321.
- [11] F. Blin, S. G. Leary, G. B. Deacon, P. C. Junk, M. Forsyth, *Corros. Sci.* **2006**, *48*, 404–419.
- [12] Y. Peng, A. E. Hughes, G. B. Deacon, P. C. Junk, B. R. W. Hinton, M. Forsyth, J. I. Mardel, A. E. Somers, *Corros. Sci.* **2018**, *145*, 199–211.
- [13] V. P. Vithana, Z. Guo, G. B. Deacon, A. E. Somers, P. C. Junk, *Molecules* **2022**, *27*, 8836 (1–16).
- [14] J. Moon, Z. Guo, O. A. Beaumont, S. Hamilton, G. Bousrez, E. Mottram, J. Wang, A. E. Somers, G. B. Deacon, P. C. Junk, *New J. Chem.* **2023**, *47*, 16843–16854.
- [15] A. E. Somers, B. R. W. Hinton, C. de Bruin-Dickason, G. B. Deacon, P. C. Junk, M. Forsyth, *Corros. Sci.* **2018**, *139*, 430–437.
- [16] V. P. Vithana, Z. Guo, G. B. Deacon, A. E. Somers, P. C. Junk, *New J. Chem.* **2022**, *46*, 19104–19111.
- [17] R. D. Shannon, *Acta Crystallogr. A* **1976**, *32*, 751–767.
- [18] C. F. MacRae, I. Sovago, S. J. Cottrell, P. T. A. Galek, P. McCabe, E. Pidcock, M. Platings, G. P. Shields, J. S. Stevens, M. Towler, P. A. Wood, *J. Appl. Crystallogr.* **2020**, *53*, 226–235.
- [19] T. M. McPhillips, S. E. McPhillips, H. J. Chiu, A. E. Cohen, A. M. Deacon, P. J. Ellis, E. Garman, A. Gonzalez, N. K. Sauter, R. P. Phizackerley, S. M. Soltis, P. Kuhn, *J. Synchrotron Radiat.* **2002**, *9*, 401–406.
- [20] W. Kabsch, *J. Appl. Crystallogr.* **1993**, *26*, 795–800.
- [21] G. M. Sheldrick, *Acta Crystallographica Section C* **2015**, *71*, 3–8.
- [22] O. V. Dolomanov, L. J. Bourhis, R. J. Gildea, J. A. K. Howard, H. Puschmann, *J. Appl. Crystallogr.* **2009**, *42*, 339–341.
- [23] *American-Standard-Test-Methods in ASTM G31-72*, Philadelphia, USA, **2004**.
- [24] N. P. Cowieson, D. Aragao, M. Clift, D. J. Ericsson, C. Gee, S. J. Harrop, N. Mudie, S. Panjkar, J. R. Price, A. Riboldi-Tunnicliffe, R. Williamson, T. Caradoc-Davies, *J. Synchrotron Radiat.* **2015**, *22*, 187–190.

Manuscript received: November 27, 2023  
Revised manuscript received: January 2, 2024  
Accepted manuscript online: January 5, 2024  
Version of record online: January 15, 2024